Available online at www.sciencedirect.com
ScienceDirect
Trans. Nonferrous Met. Soc. China 34(2024) 378−391
Transactions of Nonferrous Metals Society of China
www.tnmsc.cn

Effect of porosity and α-Al(Fe/Mn)Si phase on ductility of high-pressure die-casting Al−7Si−0.2Mg alloy

Yu-tong YANG[1,2], Shi-yao HUANG[2,3], Jiang ZHENG[4], Li YANG[1], Xiao-nong CHENG[2,5], Rui-kai CHEN[6], Wei-jian HAN[2,3]

1. Chemistry Department, Xi'an Jiaotong-Liverpool University, Suzhou 215000, China;
2. Yangtze Delta Region Institute of Advanced Materials, Suzhou 215000, China;
3. Key Laboratory for Light-weight Materials, Nanjing Tech University, Nanjing 210009, China;
4. College of Materials Science and Engineering, Chongqing University, Chongqing 400044, China;
5. School of Materials Science and Engineering, Jiangsu University, Zhenjiang 212013, China;
6. IM Motors, Shanghai 200020, China

Received 20 June 2022; accepted 14 October 2022

Abstract: High-pressure die-casting (HPDC) was used to develop two sizes of Al−7Si−0.2Mg (mass fraction, %) thin-plates with similar composition. Thin-plate castings with varying degrees of porosities and uneven microstructures were obtained and their effects on ductility were investigated. The results showed that the elongations of specimens from different castings and different positions fluctuated greatly (9.7%−17.9%). Elongation dropped sharply when specimens contained large porosities, which could be ascribed to stress concentration due to the reduction of the effective bearing area. However, for samples with small porosities, α-Al(Fe/Mn)Si phase cracked prior to eutectic phase during plastic deformation. The number density of α-Al(Fe/Mn)Si phase played an important role in the fluctuation of elongation, and specimens with higher number density of α-Al(Fe/Mn)Si particles exhibited deteriorated elongations. In addition, the increase in the number density of α-Al(Fe/Mn)Si phase was attributed to local higher cooling rates.
Key words: high-pressure die-casting; Al−7Si−0.2Mg alloy; porosity; α-Al(Fe/Mn)Si phase; ductility

1 Introduction

In recent years, proportion of lightweight materials used in vehicles has further increased to achieve higher targets of light weight and fuel-economy. Recently, high-pressure die-casting (HPDC) process has received considerable attention because of its high efficiency and short process. Al−7Si−0.2Mg (mass fraction, %) alloy is one of the most widely used non-heat treatment HPDC Al−Si alloys. The as-cast Al−7Si−0.2Mg alloy exhibits similar plasticity compared with traditional heat treatment HPDC Al−Si alloys such as Al−10Si−0.6Mn−0.4Mg, and it can avoid the problem of deformation caused by heat treatment [1,2].

HPDC Al−Si alloy shows a significant variation of mechanical properties, especially ductility [3]. Researchers have carried out a lot of studies to look into the fluctuation of elongation, and it is generally believed that the fluctuation is related to porosities [4,5]. LEE et al [6,7] found that crack preferentially expanded along regions of clusters of pores in the fracture process, and the elongation was related to the area fraction of porosities. LIU et al [8] characterized the three-dimensional morphologies of porosities in the rod tensile specimen using computed tomography (CT), and pointed out that the maximum porosity size was the main factor that affects the fracture location and

Corresponding author: Jiang ZHENG, E-mail: jzheng@cqu.edu.cn; Li YANG, E-mail: li.yang@xjtlu.edu.cn
DOI: 10.1016/S1003-6326(23)66405-2

elongation of tensile specimens. WEILER and WOOD [9] studied the effect of pore size and location on tensile fracture via finite element simulations. HU et al [10] found that wall thickness significantly affected the type and distribution of porosities in the specimen, and gas pores turned into shrinkage pores with increasing thickness which affected the elongation. However, these porosity-oriented studies have not taken the effect of microstructure into account. The synergistic effect of the microstructure and porosities on elongation has rarely been studied.

Studies indicated that the microstructures of HPDC alloys which are highly dependent on chemical compositions show a profound effect on their elongations. For instance, the as-cast microstructure will transfer from α(Al) dominant to eutectic dominant with increasing Si content, resulting in the increased strength but decreased elongation [11]. Sr element has a significant modification effect on eutectic phase. Compared with coarse flake-like eutectic Si particles, fine fibrous eutectic Si particles can suppress the crack initiation and propagation effectively caused by stress concentration, which will improve its plasticity [12]. The type and morphology of the Fe-rich phase also affect the elongation of the HPDC component [13], dodecahedral α-Al(Fe/Mn)Si replaces acicular β-AlFeSi with the addition of Mn, which can also improve the elongation [14]. However, it was found that even if the Fe-rich phase was modified by adding Mn, a large amount of α-Al(Fe/Mn)Si phases still exist at interdendritic, which will induce crack initiation [15]. Although studies have implied that the Fe-rich phase has an adverse effect on the repeatability of mechanical properties of Al−Mg alloys [16−18], the influence of α-Al(Fe/Mn)Si phases on cracking behavior of HPDC Al−7Si−0.2Mg alloy is still unclear. In addition, existing studies mainly focused on the effect of adjusting alloy elements on microstructures. The causes of local microstructure differences and their effects on mechanical properties of HPDC castings are still unclear.

The aim of the current work is to reveal the effect of porosity and α-Al(Fe/Mn)Si phase on ductility of HPDC Al−7Si−0.2Mg Alloy. In this work, two batches of HPDC Al−7Si−0.2Mg alloy thin-plates with the same composition were prepared, and tensile specimens were cut from two batches of HPDC thin-plates at different positions of the same thin-plate to obtain different microstructures and porosities. The influences of α-Al(Fe/Mn)Si phase, eutectic phase and porosities on the elongation were studied. The key processing parameter affecting the amount of formation of α-Al(Fe/Mn)Si phases with different number densities for the same composition was also discussed.

2 Experimental

Two batches of HPDC Al−Si alloy thin-plates with similar compositions but different sizes were employed in this study. HPDC A01 thin-plates were provided by CSMET® with a size of 100 mm × 300 mm, and thickness of 2.9 mm. With reference to the composition of the A01 alloy, multiple pieces of A02 alloy thin-plates were prepared by HPDC process with a size of 40 mm × 200 mm, and thickness of 2.5 mm, numbered as $1^{\#}$−$35^{\#}$. The process parameters of HPDC are given in Table 1. The chemical compositions of A01 and A02 were tested by inductive coupled plasma emission spectrometer (ICP), and the results are given in Table 2.

Table 1 Process parameters of HPDC

Alloy	Pouring temperature/ ℃	Die temperature/ ℃	Casting pressure/ MPa	Shoot speed/ ($m \cdot s^{-1}$)
A01	685−700	180−200	84	2.5
A02	685−700	180−200	85	2.5

Table 2 Chemical compositions of A01 and A02 alloys (wt.%)

Alloy	Si	Mn	Mg	Fe	Ti	Cu	Sr	Al
A01	6.499	0.600	0.188	0.102	0.074	0.001	0.009	Bal.
A02	6.609	0.623	0.176	0.159	0.080	0.001	0.003	Bal.

Standard subsize tensile specimens were machined in accordance with ASTM standard B557—15 to test the quasi-static tensile (0.8 mm/min) properties of A01 and A02 under as-cast condition. Figure 1 displays the location and size of tensile test specimens. Six tensile samples of A01 were taken from the same thin-plate, numbered $1^{\#}$−$6^{\#}$. For A02 alloy, six samples were prepared, each sample was cut from the centre of thin-plate. Room temperature

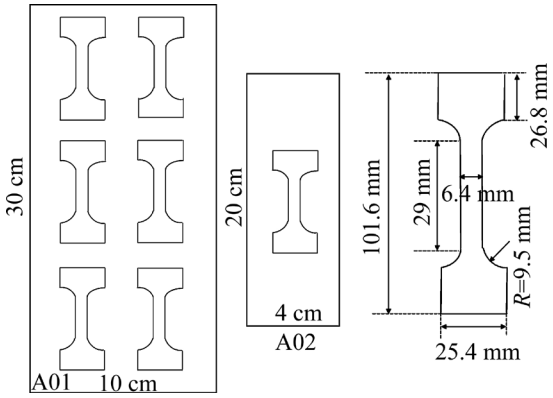

Fig. 1 Sampling location and size of A01 and A02 tensile test specimens

tensile tests were carried out on an Instron 5982 tensile machine.

Bruker D8 Discover X-ray diffractometer (XRD) and Jmat-pro software were used to examine phases and calculate phases precipitation during the solidification, respectively. The metallographic specimens were all cut and observed along the thickness direction. After mounting and mechanical grinding, the final polishing was performed using 0.03 μm oxide-polish silica suspension (OP−S), and then the samples were etched in a solution composed of 0.5 mL HF and 100 mL H_2O. The identification of the microstructure and phases was performed using a Zeiss light optical microscopy (LOM), and Zeiss GeminiSEM300 scanning electron microscope (SEM) with an energy dispersive spectroscopy (EDS). Porosities on fracture surfaces were observed by SEM and the porosity area was defined by Image-pro software.

3 Results

3.1 Thermodynamic calculation and XRD results of experimental alloys

Figure 2 demonstrates the phase transition diagram of Al−7Si−0.2Mg alloy during equilibrium solidification process. It can be seen that α(Al) dendrites start to precipitate from the liquid at 616.77 °C and the mass fraction reaches a peak value of about 92.8% at 567.12 °C. The AlFeSi phase (Fe-rich phase) has a high melting point, which precipitates at about 609 °C and increases with decreasing temperature. Eutectic Si phase is formed at 573.7 °C as a result of eutectic reaction. At 477 °C, a small amount of β-Mg_2Si phase begins to form. Table 3 shows the phase compositions of A01 and A02 at room temperature. It illustrates that Fe-rich phase content of A02 is slightly higher than that of A01 as a result of higher Fe content. Moreover, the contents of eutectic Si phase, β-Mg_2Si phase and Al_3Ti phase are almost similar. Figure 3 illustrates the XRD patterns of A01 and A02, which shows that the two alloys are mainly composed of α(Al) matrix, eutectic Si phase, β-Mg_2Si phase and Fe-rich phase.

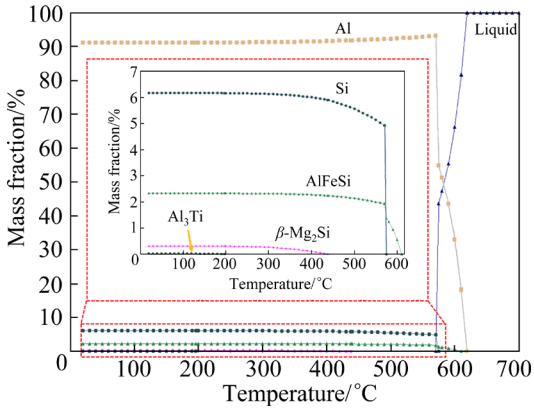

Fig. 2 Calculated phase fractions during equilibrium solidification process of Al−7Si−0.2Mg alloy

Table 3 Calculated phase fractions of A01 and A02 at room temperature (wt.%)

Alloy	Al	Si	β-Mg_2Si	Fe-rich phase	Al_3Ti
A01	90.99	6.18	0.30	2.34	0.20
A02	90.62	6.27	0.28	2.61	0.22

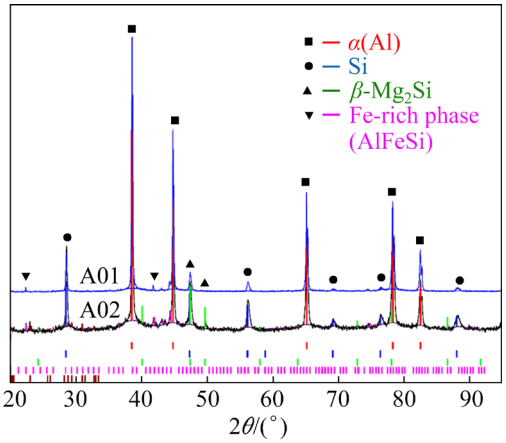

Fig. 3 XRD patterns of A01 and A02

3.2 Microstructure of as-cast sample

Figure 4 presents the metallographic images of Samples A01-2 and A02-19. The microstructures in the two alloys indicate heterogeneous through-

thickness distribution. From outside to inside, there are fine-grained area, segregation band and externally solidified crystals (ESC) enrichment area, respectively [19]. Studies show that the surface layers with fine grain and high supersaturation can improve the strength−plasticity synergy [20]. The formation of the segregation band is related to the die-casting process [21,22]. Local slip theory of dendrite network shows that the position of the bands will move toward the die wall with increasing die temperature and external fraction of solid (f_s^{ESC}) [23]. Comparing Figs. 4(a) with (b), the A01-2 alloy contains higher proportion of ESC, which may result in segregation band moving toward the surface and reducing the width of surface layer.

Figure 5 presents the SEM images and EDS results of second phases in A01-2 and A02-19. According to Figs. 5(a) and (b), both A01 and A02 exhibit fine coral-like eutectic Si particles, which is mainly attributed to the modification of Si particles by Sr and the high cooling rate of HPDC [24]. The addition of Sr can change the morphology of eutectic Si from strip-like to coral-like or granular,

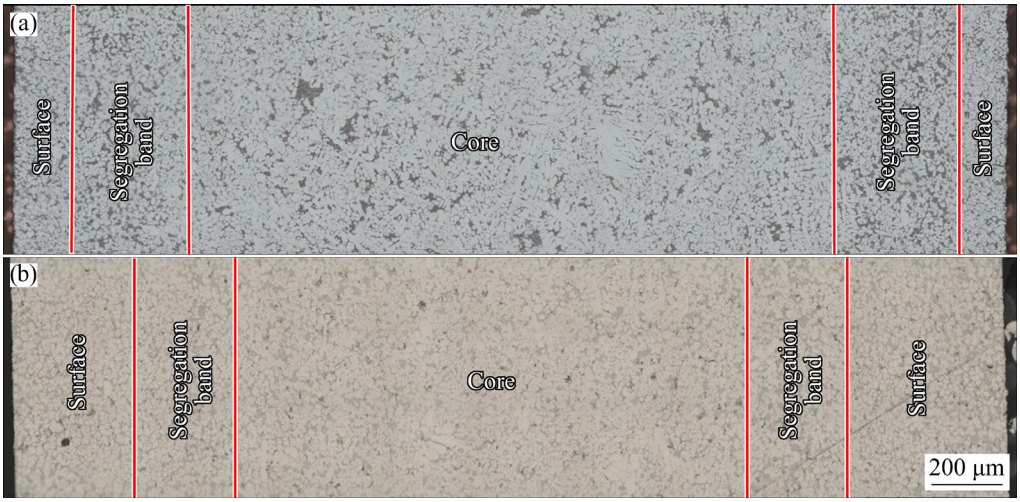

Fig. 4 Microstructures of A01-2 (a) and A02-19 (b) along thickness direction

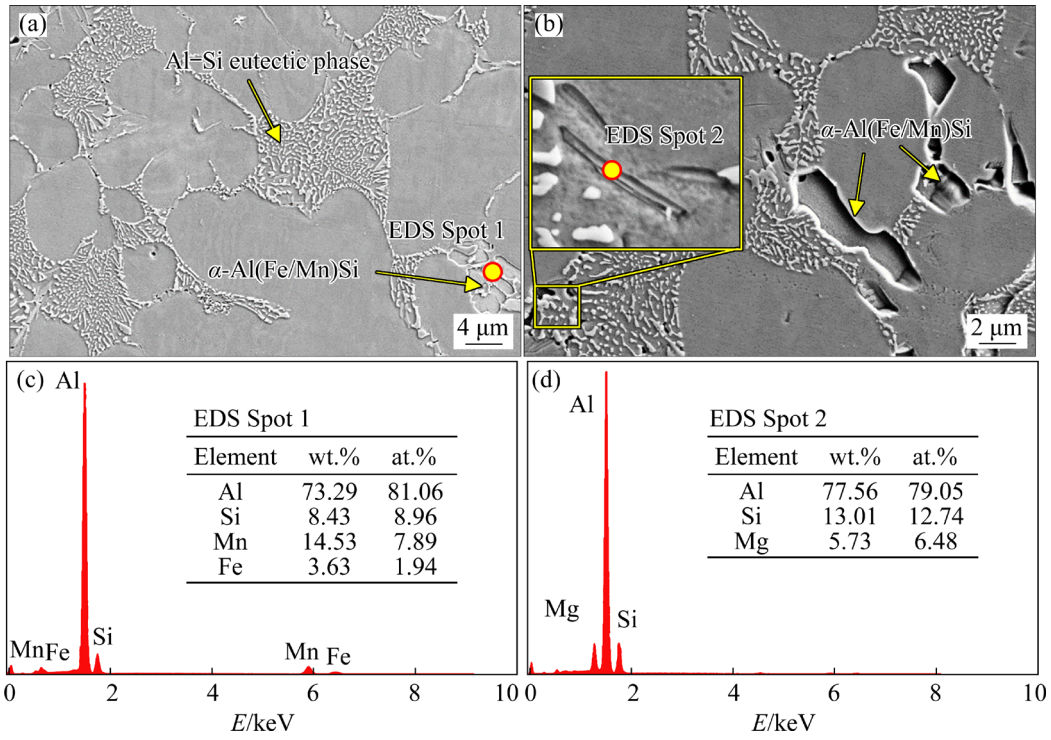

EDS Spot 1

Element	wt.%	at.%
Al	73.29	81.06
Si	8.43	8.96
Mn	14.53	7.89
Fe	3.63	1.94

EDS Spot 2

Element	wt.%	at.%
Al	77.56	79.05
Si	13.01	12.74
Mg	5.73	6.48

Fig. 5 SEM images (a, b) and EDS results (c, d) of different samples: (a) A01-2; (b) A02-19; (c) Spot 1 in (a); (d) Spot 2 in (b)

which is beneficial to improving the elongation of the alloy due to the reduced stress concentration. In addition, the ultrafine quaternary eutectic with much finer structure can reduce the tendency of stress concentration, which may improve the tensile strength [25].

β-Mg_2Si phase was also found in the eutectic phase, as shown in Fig. 5(b), and Fig. 5(d) displays the EDS result. The trace addition of Mg can combine with Si to form hard and brittle β-Mg_2Si phase, which has a strengthening effect. However, excessive brittle β-Mg_2Si phase will deteriorate the elongation of the alloys [26,27]. Therefore, the Mg content of HPDC Al−Si alloys is usually controlled at about 0.2 wt.% in order to obtain a good combination of strength and toughness.

Figures 5(a) and (b) illustrate the Fe-rich phases found in A01 and A02, respectively, each with a size of 5−10 μm. The EDS results in Fig. 5(c) demonstrate that these Fe-rich phases contain Fe and Mn elements. For hypoeutectic Al−Si alloys containing Fe and Mn, there are mainly three types of Fe-rich phases, specifically α-Al(Fe/Mn)Si, β-Al_5FeSi and α-Al_8Fe_2Si, produced under different Fe/Mn mass ratios and cooling conditions [28]. For HPDC Al−Si−Mn−Mg alloys with a Mn/Fe mass ratio of 0.5−0.6, the type of Fe-rich phase is commonly body centred cubic α-Al(Fe/Mn)Si [29]. The morphology appears as star-like, hexagonal or dendritic crystals according to different Fe/Mn mass ratios [30−32].

In summary, based on SEM observations coupled with EDS analyses, the microstructure of the as-cast A01 and A02 alloys mainly consists of α(Al) matrix, eutectic silicon, β-Mg_2Si phase and α-Al(Fe/Mn)Si phase.

3.3 Mechanical behaviour

Tensile properties of the as-cast A01 and A02 alloys are shown in Fig. 6. The average yield strength (YS), ultimate tensile strength (UTS), and elongation (EL) of the as-cast A01 are 125.1 MPa, 265.0 MPa and 14.8%, respectively, while those of A02 are 118.5 MPa, 258.7 MPa and 11.0%, respectively. For both A01 and A02, the YS and UTS did not show significant scatters, while the EL exhibited considerable variation. The ELs of A01 fluctuated between 10.3% and 17.9%, while those of A02 scattered between 9.6% and 12.7%.

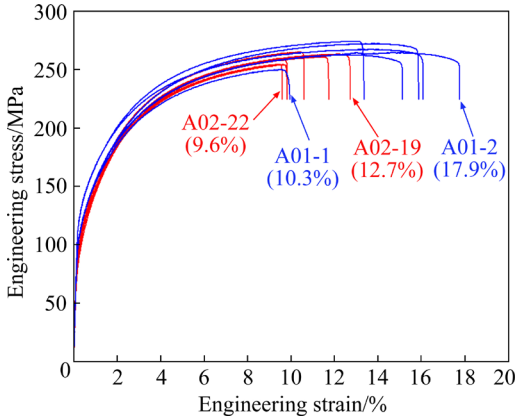

Fig. 6 Stress−strain curves of as-cast A01 and A02 at room temperature (The curves of Samples A01-1, A01-2, A02-19, and A02-22 are indicated by arrows and will be analyzed in detail, while the other curves are not labeled)

3.4 Fracture behavior

SEM observations were performed to analyze the fracture behaviors of Samples A01-2 and A02-19. Figures 7(a) and (b) show the SEM fractographs of A01-2. Dimples and tearing edges were observed on the fracture surfaces, corresponding to excellent ductility of Sample A01-2. Large area fraction of eutectic region was observed in Fig. 7(a), EDS result (Fig. 7(e)) confirmed the eutectic Si particles on the fracture surface. Some porosities such as tiny gas pores (Fig. 7(b)) were observed. The existence of gas pores could induce pre-mature fracture and resultantly reduce ductility [33].

Figures 7(c) and (d) demonstrate the SEM fractographs of A02-19. Compared with A01-2, however, more tearing edges were observed on the fracture of A02-19, as well as tiny dimples. EDS result (Fig. 7(f)) shows that α-Al(Fe/Mn)Si phases located at the bottom of the dimples, and these dimples are comparable in size to the α-Al(Fe/Mn)Si phase particles, indicating that the cracking and debonding of these particles played a crucial role in the damage mechanism, leading to the fracture of A02-19, which was also reported in Ref. [25]. Small shrinkage pores were also observed on the fracture surface (Fig. 7(d)).

4 Discussion

4.1 Effect of porosities on elongation

In order to reveal the influence of porosities on ductility, the relationship between porosity area and

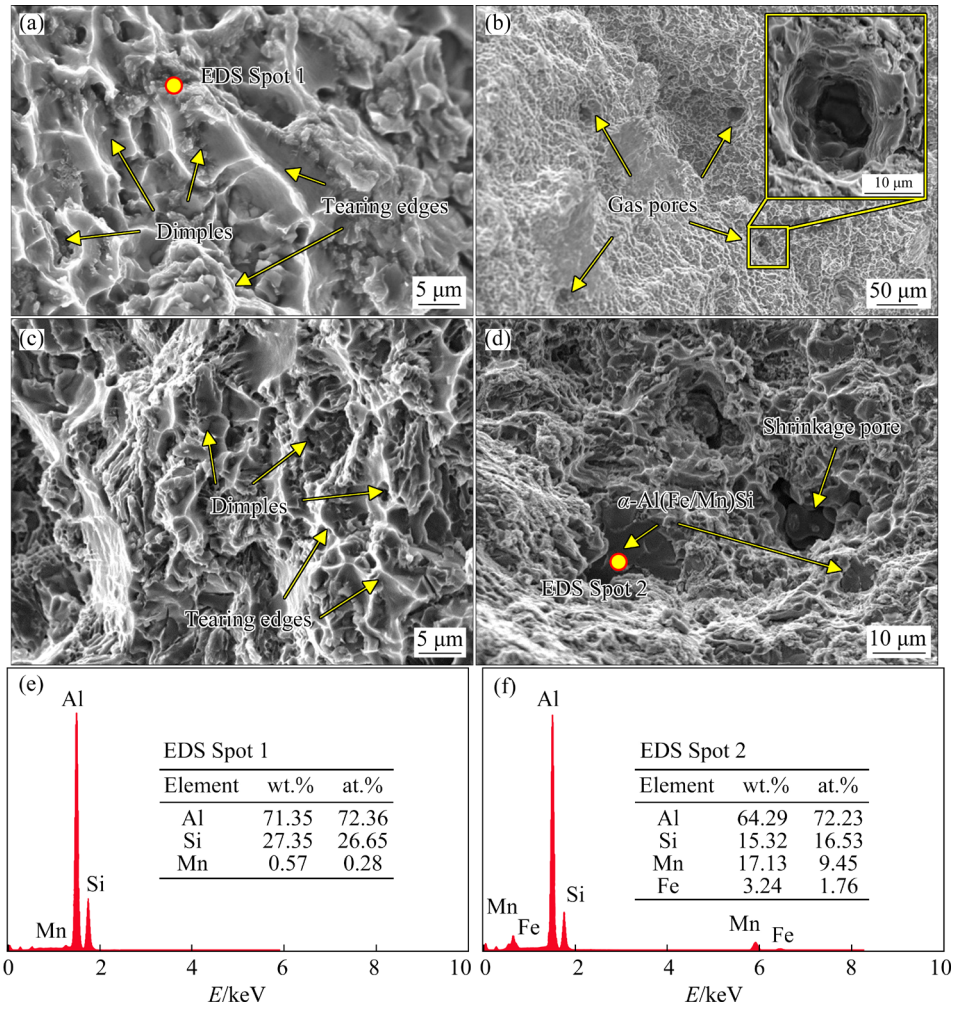

Fig. 7 SEM fractographs and EDS results of A01-2 and A02-19: (a) SEM morphology of A01-2; (b) Gas pores of A01-2; (c) Morphology of A02-19; (d) Shrinkage pore and α-Al(Fe/Mn)Si phase of A02-19; (e) EDS data of Spot 1 in (a); (f) EDS data of Spot 2 in (d)

elongation needs to be established. All shrinkage pores and gas pores on each fracture surface were observed by SEM, and total porosity area was measured by Image-Pro software as demonstrated in Fig. 8. Figure 9 demonstrates the elongation as a function of total porosity area on the fracture surface of A01 and A02 tensile samples. The samples can be divided into two groups, namely, the samples with small total porosity area (red marked region) and the samples with large total porosity area (blue marked region). Samples in the blue marked area present significantly lower elongation, and the elongation decreases with increasing the total porosity area. It can be explained by Eq. (1) [34]:

$$\sigma_{\max}=\frac{\alpha F}{S_0(1-\mu)} \tag{1}$$

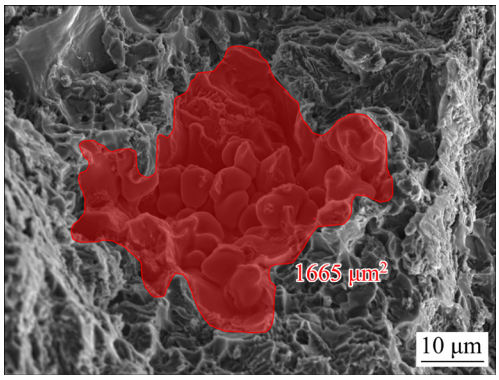

Fig. 8 Total porosity area measured by Image-Pro software

where $\sigma_{\max}$ is the maximum stress, α is the stress concentration factor of the porosities, F is the tensile force, S_0 is the cross-sectional area, and μ is the area fraction of porosities. Since porosities are found on the fracture surfaces of most tensile

specimens, μ in Eq. (1) is greater than 0. This means that stress concentrated near the porosities, which caused crack initiation and accelerated the fracture process. Therefore, the elongation was significantly reduced for samples with a large number of porosities.

Contrarily, the average elongation of samples with lower porosity (in the red marked area) is higher than that of samples with higher porosity (the blue marked area). However, the samples with few porosities observed on the fracture surfaces exhibit obvious variation in ductility (12.7%−17.9%).

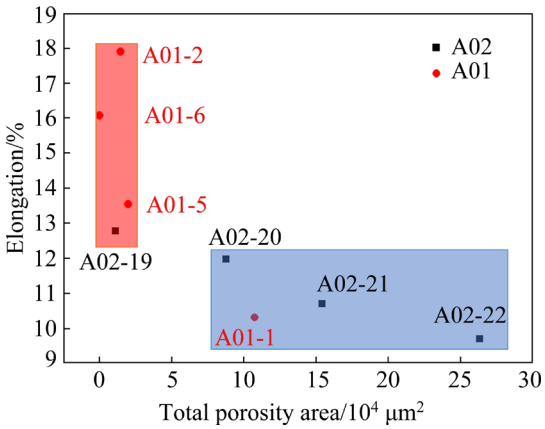

Fig. 9 Correlation between elongation and total porosity area

4.2 Effect of second phases on cracking behavior

Figure 10 displays the SEM morphologies of the regions near the fracture surfaces of Samples A02-19 and A01-2. The schematic diagram of the observation position is displayed in Fig. 11. As depicted in Fig. 10, it can be clearly observed that a large number of cracks concentrate near Al–Si eutectic phase. Weak bonding force between eutectic Si and eutectic Al induces crack initiation and propagation along the interface rapidly. In addition, coarse α-Al(Fe/Mn)Si phases also intensify crack propagation as displayed in Fig. 10, which deteriorates the mechanical properties of the alloys. Therefore, both eutectic phase and α-Al(Fe/Mn)Si phase play an important role in the initiation and propagation of cracks, and ultimately affect the ductility.

Therefore, in order to identify the phase governing elongation of the samples exclusively containing small porosity, Samples A02-19 and A01-2, which had comparable areas of porosity and

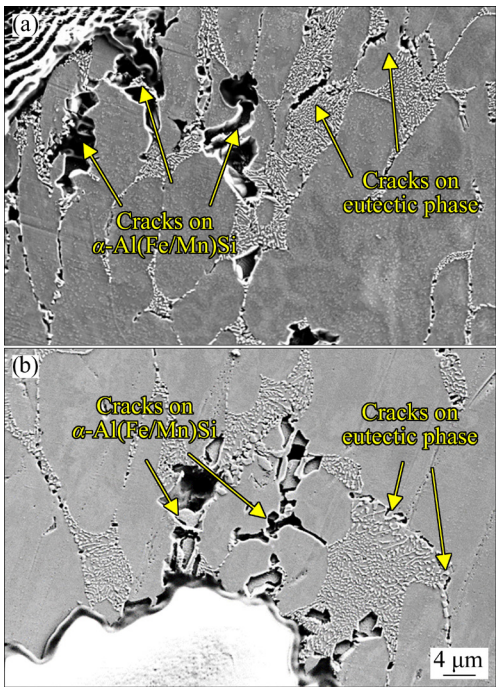

Fig. 10 SEM images of longitudinal sections nearby tensile fracture: (a) A02-19; (b) A01-2

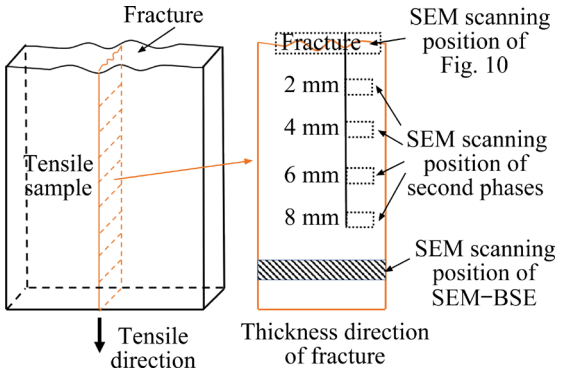

Fig. 11 Schematic diagram of observation position

similar size of the largest pores on the fracture surfaces, were selected and the fracture parts of tensile specimens were cut along the tensile direction. Necking occurred in the gauge length segment during plastic deformation, and the necking zone presented heterogeneous deformation. The largest strain was generally located in the fracture region, and decreased gradually with increasing distance from fracture region [35]. In order to observe crack initiation and propagation with increasing strain, eutectic phase and α-Al(Fe/Mn)Si phase at different distances from the fracture surfaces were observed using SEM.

SEM fractographs of Sample A02-19, specifically in its longitudinal section, are depicted

in Figs. 12(a, c, e, g), α-Al(Fe/Mn)Si particles at distances of 2−8 mm from the fracture surface can be clearly observed to break into pieces, and crack propagation direction was perpendicular to the tensile direction. At a distance of 2 mm from the fracture (Fig. 12(a)), decohesion was found on the eutectic phase which mainly extended along the interface between eutectic Si particles and eutectic Al. Inversely, no obvious cracks were found on Al−Si eutectic phase at distances of 4, 6 and 8 mm from the fracture (Figs. 12(c, e, g)). Figures 12(b, d, f, h) demonstrate the microstructure of Sample A01-2, all α-Al(Fe/Mn)Si phases at different distances from the fracture were fractured. As seen in Figs. 12(f, h), some discontinuous pores were found around eutectic Si particles, then multiple holes connected and expanded along the interfaces where microcracks formed (Fig. 12(d)).

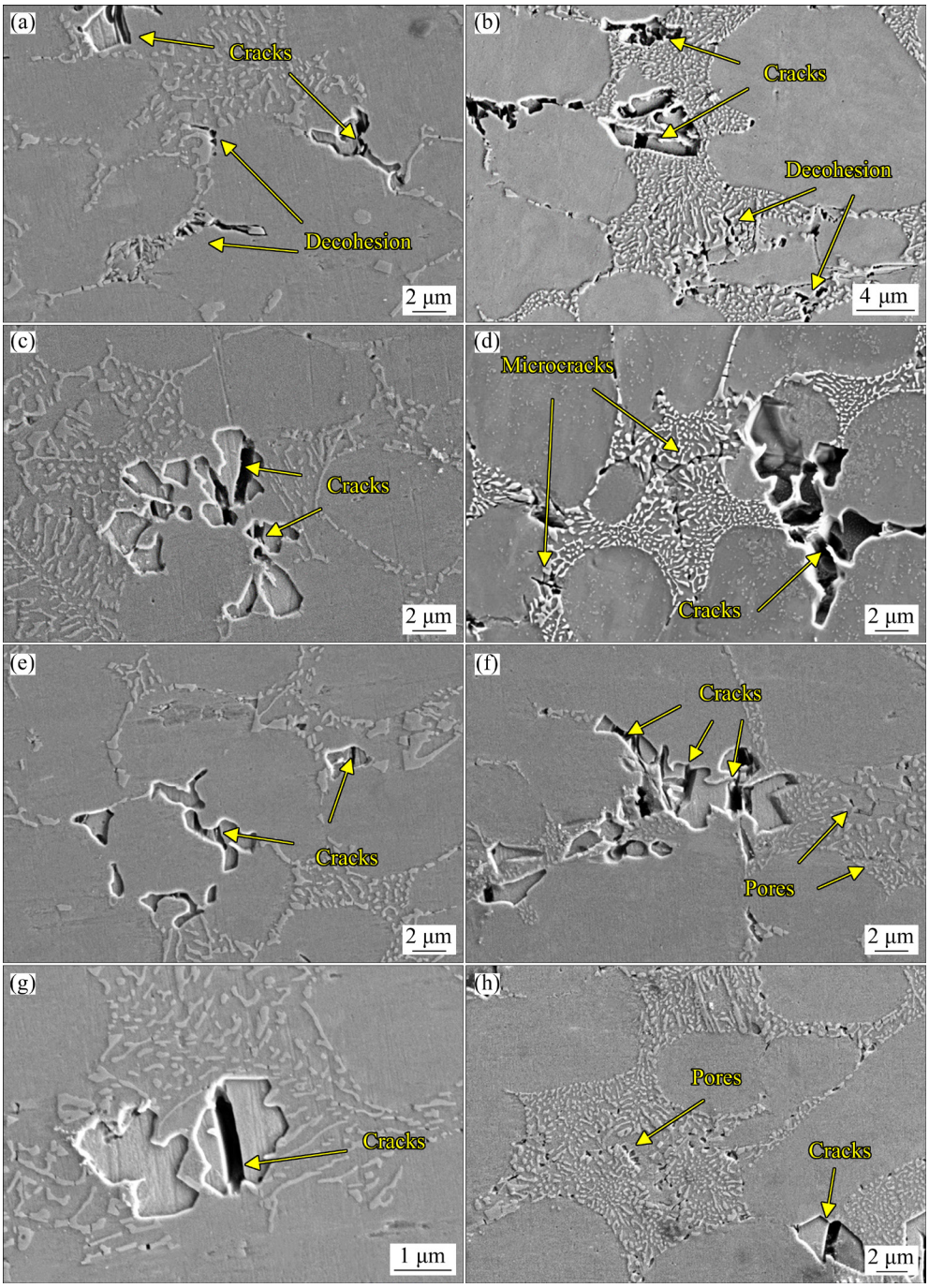

Fig. 12 SEM images showing fracture of eutectic phase and α-Al(Fe/Mn)Si at distances of 2 mm (a), 4 mm (c), 6 mm (e) and 8 mm (g) from fracture surface of A02-19, and 2 mm (b), 4 mm (d), 6 mm (f) and 8 mm (h) from fracture surface of A01-2

Finally, a large area of Si particles exfoliated, leading to complete failure of eutectic phase (Fig. 12(b)). Based on these analyses, it can be seen that α-Al(Fe/Mn)Si phase ruptured before the Al−Si eutectic phase with increasing the strain. The cracking of eutectic phase can be attributed to interface decohesion.

Compared with fine fibrous eutectic silicon, coarse polygonal α-Al(Fe/Mn)Si phase facilitated stress concentration and crack initiation. The relationship between Young's modulus and Poisson's ratio of second phases as a function of temperature was calculated by Jmat-Pro software. The calculation results of Young's modulus are very close to the reported results [14,36]. As depicted in Fig. 13, α-Al(Fe/Mn)Si phase shows the highest Young's modulus and the lowest Poisson's ratio. This means that the mismatch between α-Al(Fe/Mn)Si phase and the matrix generated in the process of plastic deformation, then stress concentration induced the earliest crack source [34]. After that, the cracking induced by α-Al(Fe/Mn)Si phase led to a decrease in the effective bearing area of the plane perpendicular to tensile direction, finally resulting in elongation reduction.

To study the influence of α-Al(Fe/Mn)Si on elongation, three tensile specimens (A01-2, A01-5 and A02-19) with low total porosity area (Fig. 9) were selected. SEM−BSE was used to analyze the morphology and spatial distribution of α-Al(Fe/Mn)Si particles, and the results are displayed in Fig. 14. Figure 14(a) shows the SEM−BSE image of Sample A01-2, in which the bright areas are α-Al(Fe/Mn)Si particles. Figures 14(b) and (c) show the SEM−BSE images of Samples A01-5 and A02-19, respectively. It can be clearly observed that

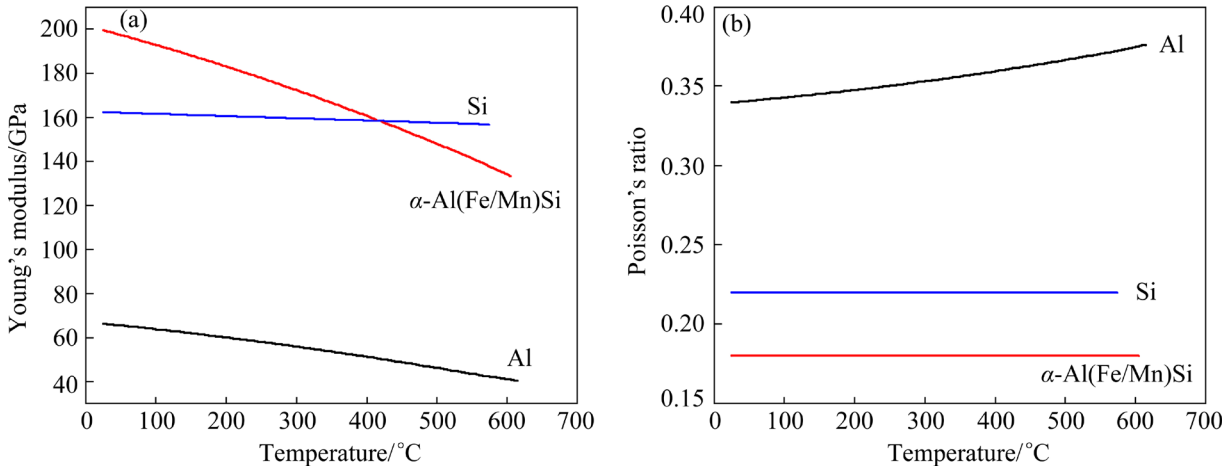

Fig. 13 Young's modulus (a) and Poisson's ratio (b) of second phases as function of temperature calculated by Jmat-Pro sofware

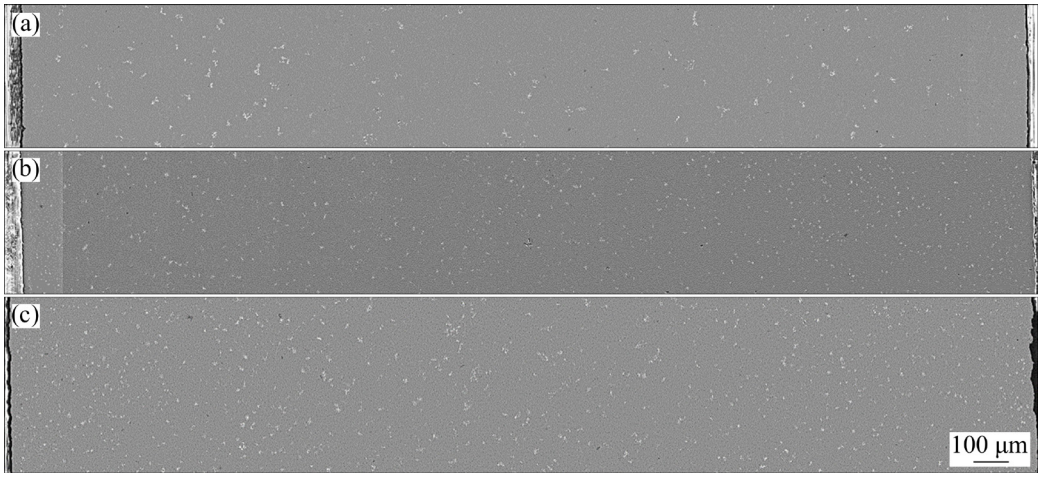

Fig. 14 SEM−BSE microstructures of A01-2 (a), A01-5 (b) and A02-19 (c) along thickness direction

the number density of α-Al(Fe/Mn)Si particles in Sample A01-5 is significantly higher than that in Sample A01-2. Compared with the core area, α-Al(Fe/Mn)Si particles near the surface and the segregation zone are characterized by small size and high density.

Quantitative analysis was carried out using Image-Pro software to study the number density of α-Al(Fe/Mn)Si particles. Figure 15(a) presents the variation law of α-Al(Fe/Mn)Si number density with distance from surface. It can be seen that the overall number density of α-Al(Fe/Mn)Si in Sample A01-2 is significantly lower than that in the counterpart. The number density curves of Samples A01-5 and A02-19 show the same trend, that is, density is very high on surface, decreases sharply at segregation band, and then decreases gradually towards the core. Overall, Sample A02-19 has the highest number density of α-Al(Fe/Mn)Si phase. Figure 15(b) shows that elongation decreases with increasing number density of α-Al(Fe/Mn)Si particles. This implies that for samples with small total porosity area, the number density of α-Al(Fe/Mn)Si phase plays a leading role in the fluctuation of elongation.

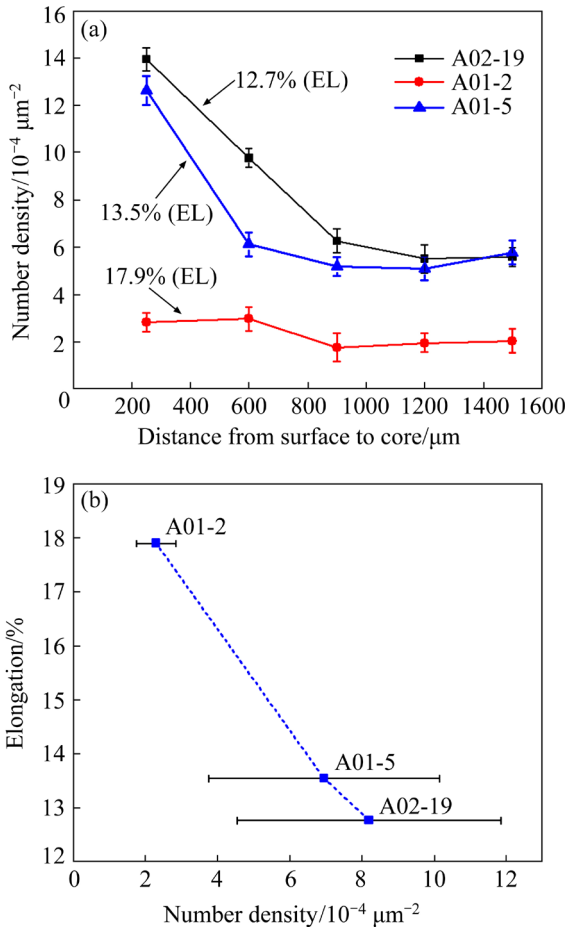

Fig. 15 Number density of α-Al(Fe/Mn)Si particles as function of distance from surface to core (a) and elongation as function of number density (b)

4.3 Reasons for formation of α-Al(Fe/Mn)Si phases with different number densities

The α-Al(Fe/Mn)Si phase precipitates from the liquid phase during solidification process, which includes two steps: nucleation and growth. Due to the large degree of undercooling required for uniform nucleation (about $0.2T_m$, T_m is the melting point of material), solidification of metals is usually a heterogeneous nucleation, and the total Gibbs free energy change (ΔG) in the system can be expressed as Eq. (2) [37]:

$$\Delta G=\left(\frac{4}{3}\pi r^3\Delta G_v+4\pi r^2\sigma_{aL}\right)\cdot\left(\frac{2-3\cos\theta+\cos\theta^3}{4}\right)=\left(\frac{4}{3}\pi r^3\Delta G_v+4\pi r^2\sigma_{aL}\right)f(\theta) \quad (2)$$

where r is the nucleus radius, ΔG_v is the change in Gibbs free energy per unit volume, σ_{aL} is the specific surface energy of the interface between the crystal nucleus and the liquid phase, and θ is the wetting angle. For experimental materials, ΔG_v, σ_{aL} and θ are all fixed values, so ΔG is a function of r. Equation (dG/dr)=0 is brought into Eq. (2) to obtain its critical nucleation radius (r^*)[37]:

$$r^*=-\frac{2\sigma_{aL}}{\Delta G_v}=\frac{2\sigma_{aL}T_m}{L_m\Delta T} \quad (3)$$

where L_m is the heat of fusion. Therefore, the critical nucleation radius of the second phase is determined by the degree of undercooling (ΔT). With the increase of undercooling ΔT, the critical nucleation radius r^* decreases, leading to the increasing number of second phases.

Numerous studies have found that there is a quantitative relationship between the secondary dendrite arm spacing (SDAS) and the cooling rate (C) [38]:

$$\text{SDAS}=AC^n \quad (4)$$

where A is the coefficient, n is the roughening index, and both A and n are constants for a specific

alloy (n<0). WANG and CÁCERES [39] measured n=−0.35 and A=39.4 for Al−7Si−0.4Mg. CHEN et al [40] measured n=−0.31 and A=40.5 for Al−7Si−0.36Mg. GU et al [41] measured n=−0.34 and A=39.6 for Al−8.5Si−0.3Mg−0.12Fe−0.58Mn. Since A01 and A02 have the same compositions, it can be considered that their A and n are the same, and the SDAS decreases with the increase of cooling rate. Figure 16 exhibits the SDAS from the surface to core of A02 and A01. It can be seen that the SDAS values of different samples are quite different. According to Eq. (2), A01-2 possesses the lowest cooling rate, followed by A01-5, A02-19 and A01-6.

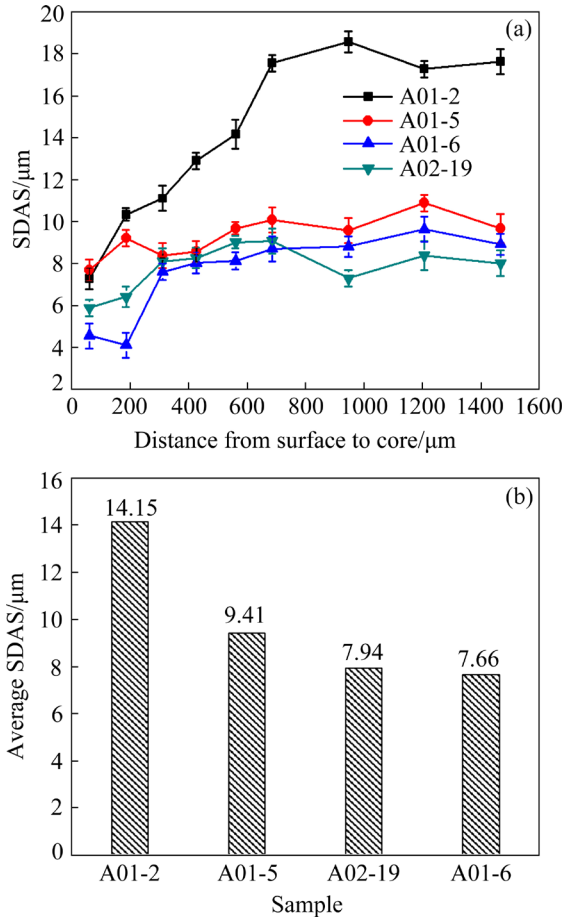

Fig. 16 Comparison of SDAS between A01 and A02: (a) SDAS from surface to core; (b) Average SDAS

The relationship between the average SDAS and number density of α-Al(Fe/Mn)Si phase is depicted in Fig. 17. It can be clearly observed that number density increases with the decrease in SDAS, suggesting that the number density of α-Al(Fe/Mn)Si phase increases with the increase of the cooling rate. This is because higher cooling rate corresponds to a larger degree of undercooling, which reduces the r^* of the α-Al(Fe/Mn)Si phase nucleus, resulting in high number density. By observing both A02 and A01 alloys, it can be found that the number density of α-Al(Fe/Mn)Si phases is much higher in the surface layer than that in the core, which is also related to the higher cooling rate.

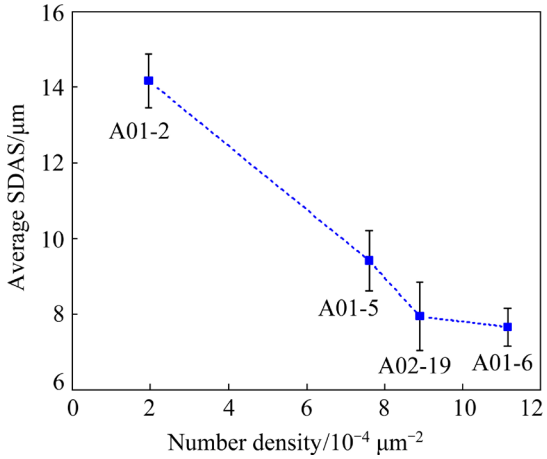

Fig. 17 Relationship between average SDAS and number density of α-Al(Fe/Mn)Si phase

The number density of α-Al(Fe/Mn)Si phase, in addition to porosities, is also an important factor that affects the elongation of HPDC alloys. Although tensile samples of A01 were taken from one thin-plate, the difference in local cooling rate resulted in uneven distribution of α-Al(Fe/Mn)Si phase, which induced the fluctuation of elongation. Therefore, in order to improve the mechanical properties of large-scale HPDC Al−Si alloy components, it is necessary to control the cooling rate at different locations to reduce the precipitation of α-Al(Fe/Mn)Si phase.

5 Conclusions

(1) The yield and tensile strengths of the two studied alloys did not exhibit substantial variations. However, the remarkable fluctuation of elongation was observed for both A01 and A02.

(2) The total porosity area has a great influence on elongation. The samples with large porosity area showed low elongations.

(3) For samples with small total porosity area, the number density of α-Al(Fe/Mn)Si phase played a leading role in the fluctuation of elongation. Brittle α-Al(Fe/Mn)Si particles acted as primary crack sources. Eutectic Si particles tended to induce

cracking subsequently. Samples with higher number density of α-Al(Fe/Mn)Si particles exhibited reduced elongation.

(4) Cooling rate is an important factor affecting the number density of α-Al(Fe/Mn)Si phase. High cooling rate led to an increase in number density, which acted as a crucial influencing factor for elongation.

CRediT authorship contribution statement

Yu-tong YANG: Methodology, Visualization, Writing − Original draft preparation; **Shi-yao HUANG:** Conceptualization, Writing − Reviewing & editing; **Jiang ZHENG:** Conceptualization, Writing − Reviewing & editing; **Li YANG:** Writing − Reviewing & editing; **Xiao-nong CHENG:** Validation; **Rui-kai CHEN:** Validation; **Wei-jian HAN:** Funding acquisition.

Declaration of competing interest

The authors declare that they have no known competing financial interests or personal relationships that could have appeared to influence the work reported in this paper.

Acknowledgments

This work was financially supported by the Fundamental Research Funds for the Central Universities, China (No. 2020CDJDPT001), and the Chongqing Natural Science Foundation, China (No. cstc2021jcyj-msxmX0699).

References

[1] YUAN Zhi-hao, GUO Zhi-peng, XIONG Shou-mei. Microstructure evolution of modified die-cast $AlSi_{10}MnMg$ alloy during solution treatment and its effect on mechanical properties [J]. Transactions of Nonferrous Metals Society of China, 2019, 29: 919−930.

[2] DERIN S, AYBARC U, BIROL Y. Effect of strontium addition on microstructure and mechanical properties of $AlSi_7Mg_{0.3}$ alloy [J]. International Journal of Metalcasting, 2017, 11: 688−695.

[3] UBERTALLI G, D′AIUTO F, PLANO S, de CARO D. High strain rate behavior of aluminum die cast components [J]. Procedia Structural Integrity, 2016, 2: 3617−3624.

[4] CÁCERES C H. On the effect of macroporosity on the tensile properties of the Al−7%Si−0.4%Mg casting alloy [J]. Scripta Metallurgica et Materialia, 1995, 32: 1851−1856.

[5] WEILER J P, WOOD J T, KLASSEN R J, MAIRE E, BERKMORTEL R, WANG G. Relationship between internal porosity and fracture strength of die-cast magnesium AM60B alloy [J]. Materials Science and Engineering A, 2005, 395: 315−322.

[6] LEE S G, PATEL G R, GOKHALE A M, SREERANGANATHAN A, HORSTEMEYER M F. Variability in the tensile ductility of high-pressure die-cast AM50 Mg-alloy [J]. Scripta Materialia, 2005, 53: 851−856.

[7] LEE S G, PATEL G R, GOKHALE A M, SREERANGANATHAN A, HORSTEMEYER M F. Quantitative fractographic analysis of variability in the tensile ductility of high-pressure die-cast AE44 Mg-alloy [J]. Materials Science and Engineering A, 2006, 427: 255−262.

[8] LIU Ru-xue, ZHENG Jiang, GODLEWSKI L, ZINDEL J, LI Mei, LI Wen-kai, HUANG Shi-yao. Influence of pore characteristics and eutectic particles on the tensile properties of Al−Si−Mn−Mg high pressure die casting alloy [J]. Materials Science and Engineering A, 2020, 783: 139280.

[9] WEILER J P, WOOD J T. Modeling fracture properties in a die-cast AM60B magnesium alloy II—The effects of the size and location of porosity determined using finite element simulations [J]. Materials Science and Engineering A, 2009, 527: 32−37.

[10] HU Qi-yao, GUO Wen-bo, ZHAO Hai-dong. Influence of wall thickness and intensification pressure on the microstructures and mechanical properties of $AlSi_7$−SiC composites fabricated by the vacuum-assisted HPDC process [J]. Materials Science and Engineering A, 2021, 819: 141470.

[11] OUTMANI I, FOUILLAND-PAILLE L, ISSELIN J, EL MANSORI M. Effect of Si, Cu and processing parameters on Al−Si−Cu HPDC castings [J]. Journal of Materials Processing Technology, 2017, 249: 559−569.

[12] GAN Jun-qi, HUANG Yu-jian, WENG Cheng, DU Jun. Effect of Sr modification on microstructure and thermal conductivity of hypoeutectic Al−Si alloys [J]. Transactions of Nonferrous Metals Society of China, 2020, 30: 2879−2890.

[13] TAYLOR J A. Iron-containing intermetallic phases in Al−Si based casting alloys [J]. Procedia Materials Science, 2012, 1: 19−33.

[14] ZHANG Xiao-zhu, WANG Dong-tao, ZHOU Yun-xuan, CHONG Xiao-yu, LI Xin-zhong, ZHANG Hai-tao, NAGAUMI H. Exploring crystal structures, stability and mechanical properties of Fe, Mn-containing intermetallics in Al−Si alloy by experiments and first-principles calculations [J]. Journal of Alloys and Compounds, 2021, 876: 160022.

[15] LIN Bo, FAN Tao, LI Hao-yu, ZHAO Yu-liang, ZHANG Wei-wen, LIU Kun. Microstructure and high temperature tensile properties of Al−Si−Cu−Mn−Fe alloys prepared by semi-solid thixoforming [J]. Transactions of Nonferrous Metals Society of China, 2021, 31: 2232−2249.

[16] YANG Hai-lin, JI Shou-xun, WATSON D, FAN Zhong-yun. Repeatability of tensile properties in high pressure die-castings of an Al−Mg−Si−Mn alloy [J]. Metals and Materials International, 2015, 21: 936−943.

[17] JI Shou-xun, YANG Hai-lin, WATSON D, FAN Zhong-yun. Weibull analysis for the repeatibility of die castings made by an Al−Mg−Si−Mn alloy [C]//Light Metals. Cham: Springer, 2016: 681−685.

[18] JI Shou-xun, YANG Wen-chao, GAO Feng, WATSON D, FAN Zhong-yun. Effect of iron in Al−Mg−Si−Mn ductile diecast alloy [C]//Light Metals. Cham: Springer, 2013: 317−322.

[19] JIAO Xiang-yi, LIU Chao-feng, WANG Jun, GUO Zhi-peng, WANG Jun-you, WANG Zhuo-ming, GAO Jun-ming, XIONG Shou-mei. On the characterization of microstructure and fracture in a high-pressure die-casting Al−10wt.%Si alloy [J]. Progress in Natural Science: Materials International, 2020, 30: 221−228.

[20] NIU Guo-dong, WANG J, LI Jin-ping, YE Jin-wen, MAO Jian. The formation mechanism of the chill fine-grain layer with high supersaturation and its influence on the mechanical properties of die casting Al−7Si−0.5Mg alloy [J]. Materials Science and Engineering A, 2012, 833: 142544.

[21] HOU Ying-ying, WU Meng-hu, TIAN Bing-hui, LI Xiao-bo, XIONG Shou-mei. Characteristics and formation mechanisms of defect bands in vacuum-assisted high-pressure die casting AE44 alloy [J]. Transactions of Nonferrous Metals Society of China, 2022, 32: 1852−1865.

[22] TIMELLI G, FABRIZI A. The effects of microstructure heterogeneities and casting defects on the mechanical properties of high-pressure die-cast $AlSi_9Cu_3$(Fe) alloys [J]. Metallurgical and Materials Transactions A, 2014, 45: 5486−5498.

[23] GOURLAY C M, DAHLE A K, LAUKLI H I. Segregation band formation in Al−Si die castings [J]. Metallurgical and Materials Transactions A, 2004, 35: 2881−2891.

[24] FARAHANY S, OURDJINI A, BAKHSHESHI-RAD H R. Microstructure, mechanical properties and corrosion behavior of Al−Si−Cu−Zn−X (X=Bi, Sb, Sr) die cast alloy [J]. Transactions of Nonferrous Metals Society of China, 2016, 26: 28−38.

[25] ZHANG Pen, LI Zhen-ming, LIU Bao-ling, DING Wen-jiang. Effect of chemical compositions on tensile behaviors of high pressure die-casting alloys Al−10Si−yCu−xMn−zFe [J]. Materials Science and Engineering A, 2016, 661: 198−210.

[26] WANG Dong-tao, ZHANG Hai-tao, NAGAUMI H, JIA Pin-feng, CUI Jian-zhong. Microstructural homogeneity, mechanical properties, and wear behavior of in situ Mg_2Si particles reinforced Al-matrix composites fabricated by hot rolling [J]. Journal of Materials Research and Technology, 2020, 9: 1882−1892.

[27] YANG Hai-lin, JI Shou-xun, YANG Wen-chao, WANG Yun, FAN Zhong-yun. Effect of Mg level on the microstructure and mechanical properties of die-cast Al−Si−Cu alloys [J]. Materials Science and Engineering A, 2015, 642: 340−350.

[28] CINKILIC E, RIDGEWAY C D, YAN X, LUO A A. A formation map of iron-containing intermetallic phases in recycled cast aluminum alloys [J]. Metallurgical and Materials Transactions A, 2019, 50: 5945−5956.

[29] JI Shou-xun, YANG Wen-chao, GAO Feng, WATSON D, FAN Zhong-yun. Effect of iron on the microstructure and mechanical property of Al−Mg−Si−Mn and Al−Mg−Si diecast alloys [J]. Materials Science and Engineering A, 2013, 564: 130−139.

[30] SEIFEDDINE S, JOHANSSON S, SVENSSON I L. The influence of cooling rate and manganese content on the β-Al_5FeSi phase formation and mechanical properties of Al−Si-based alloys [J]. Materials Science and Engineering A, 2008, 490: 385−390.

[31] LIN Chong, WU Shu-sen, LU Shu-lin, WU He-bao, CHEN Han-xin. Influence of high pressure and manganese addition on Fe-rich phases and mechanical properties of hypereutectic Al−Si alloy with rheo-squeeze casting [J]. Transactions of Nonferrous Metals Society of China, 2019, 29: 253−262.

[32] LI Zai-dao, LIMODIN N, TANDJAOUI A, QUAEGEBEUR P, OSMOND P, BALLOY D. Influence of Sr, Fe and Mn content and casting process on the microstructures and mechanical properties of $AlSi_7Cu_3$ alloy [J]. Materials Science and Engineering A, 2017, 689: 286−297.

[33] DOU Kun, LORDAN E, ZHANG Yi-jie, JACOT A, FAN Zhong-yun. A novel approach to optimize mechanical properties for aluminium alloy in high pressure die casting (HPDC) process combining experiment and modeling [J]. Journal of Materials Processing Technology, 2021, 296: 117193.

[34] LI X, XIONG S M, GUO Z P. On the porosity induced by externally solidified crystals in high-pressure die-cast of AM60B alloy and its effect on crack initiation and propagation [J]. Materials Science and Engineering A, 2015, 633: 35−41.

[35] ZHANG Ding-ni, SHANGGUAN Qian-qian, XIE Can-jun, LIU Fu. A modified Johnson−Cook model of dynamic tensile behaviors for 7075-T6 aluminum alloy [J]. Journal of Alloys and Compounds, 2015, 619: 186−194.

[36] MCSKIMIN H J, ANDREATCH P Jr. Elastic moduli of silicon vs hydrostatic pressure at 25.0 °C and −195.8 °C [J]. Journal of Applied Physics, 1964, 35: 2161−2165.

[37] CALLISTER W D, RETHWISCH D G. Materials science and engineering: An introduction [M]. New York: Wiley, 2018.

[38] EL-BEALY M, THOMAS B G. Prediction of dendrite arm spacing for low alloy steel casting processes [J]. Metallurgical and Materials Transactions B, 1996, 27: 689−693.

[39] WANG Q G, CÁCERES C H. Mg effects on the eutectic structure and tensile properties of Al−Si−Mg alloys [J]. Materials Science Forum, 1997, 242: 159−164.

[40] CHEN Rui, XU Qing-yan, LIU Bai-cheng. Cellular automaton simulation of three-dimensional dendrite growth in Al−7Si−Mg ternary aluminum alloys [J]. Computational Materials Science, 2015, 105: 90−100.

[41] GU C, RIDGEWAY C D, MOODISPAW M P, LUO A A. Multi-component numerical simulation and experimental study of dendritic growth during solidification processing [J]. Journal of Materials Processing Technology, 2020, 286: 116829.

孔隙和 α-Al(Fe/Mn)Si 相对高压压铸 Al−7Si−0.2Mg 合金塑性的影响

杨雨童[1,2]，黄诗尧[2,3]，郑 江[4]，杨 莉[1]，程晓农[2,5]，陈睿凯[6]，韩维建[2,3]

1. 西交利物浦大学 化学系，苏州 215000；
2. 长三角先进材料研究院，苏州 215000；
3. 南京工业大学 先进轻质高性能材料研究中心，南京 210009；
4. 重庆大学 材料科学与工程学院，重庆 400044；
5. 江苏大学 材料科学与工程学院，镇江 212013；
6. 智己汽车科技有限公司，上海 200020

摘 要：采用高压压铸工艺制备两批次不同尺寸的 Al−7Si−0.2Mg (质量分数, %)合金，获得显微组织和孔隙非均匀分布的薄壁铸件，并对比研究孔隙和显微组织对铸态合金塑性的影响。结果表明：不同铸件和不同位置样品的伸长率有较大波动 (9.7%~17.9%)。当合金存在大面积孔隙时，有效承载面积减小导致由孔隙产生的应力集中使合金伸长率显著降低。当合金只存在小面积孔隙时，塑性变形过程中合金中的 α-Al(Fe/Mn)Si 相先于共晶硅相发生脆性断裂，α-Al(Fe/Mn)Si 相的数量密度对伸长率的波动起主导作用，具有高数量密度 α-Al(Fe/Mn)Si 相试样的伸长率显著降低。此外，局部较高的冷却速率导致铸件 α-Al(Fe/Mn)Si 相数量密度的增加。

关键词：高压压铸；Al−7Si−0.2Mg 合金；孔隙；α-Al(Fe/Mn)Si 相；塑性

(Edited by Wei-ping CHEN)